First global distributions of nitric acid in the troposphere and the stratosphere derived from infrared satellite measurements

Catherine Wespes, Daniel Hurtmans, Hervé Herbin, Brice Barret, Solène Turquety, Juliette Hadji-Lazaro, Cathy Clerbaux, Pierre-François Coheur

First global distributions of nitric acid in the troposphere and the stratosphere derived from infrared satellite measurements

Catherine Wespes,[1] Daniel Hurtmans,[1] Hervé Herbin,[1] Brice Barret,[1,2] Solène Turquety,[3] Juliette Hadji-Lazaro,[3] Cathy Clerbaux,[1,3] and Pierre-François Coheur[1,4]

Received 31 October 2006; revised 23 February 2007; accepted 3 April 2007; published 12 July 2007.

[1] Global distributions of nitric acid (HNO_3) partial columns in the troposphere and the stratosphere are shown for the first time. HNO_3 vertical profiles are retrieved from a set of high-resolution infrared spectra, measured by the nadir-viewing Interferometric Monitor for Greenhouse Gases (IMG) instrument onboard the ADEOS satellite. Ten successive days of IMG operation in April 1997 are analyzed, yielding quasi-global distributions. We show that the IMG measurements contain between 0.7 and 1.8 independent pieces of information on the HNO_3 vertical distribution; the extent of which depends on the observed scene. In the tropics and the midlatitudes, tropospheric and stratospheric columns can be separated, whereas, in the colder polar regions, the total column is the most relevant quantity. A detailed error budget reveals that the accuracy on the profile measurements ranges from 5–15% in the stratosphere to about 20–30% in the middle troposphere, and as much as 60% in the lowermost troposphere where the measurements are less sensitive. The global distributions of tropospheric and stratospheric partial columns are presented and discussed. In the stratosphere we measure higher columns at both poles than in the intertropical belt, as expected for the period in April analyzed here. In the troposphere, the zonal distributions show elevated values nearby NO_x source regions, such as central Europe, the Eastern coast of the United States, and the North-West of India. Typical profiles with mixing ratios up to 2 ppbv in the boundary layer and 1 ppbv in the free troposphere are identified. These novel results indicate a possible role of HNO_3 in the long-range transport of active nitrogen and open promising perspectives for future space missions dedicated to atmospheric chemistry.

Citation: Wespes, C., D. Hurtmans, H. Herbin, B. Barret, S. Turquety, J. Hadji-Lazaro, C. Clerbaux, and P.-F. Coheur (2007), First global distributions of nitric acid in the troposphere and the stratosphere derived from infrared satellite measurements, *J. Geophys. Res.*, *112*, D13311, doi:10.1029/2006JD008202.

1. Introduction

[2] Nitrogen oxides play a central role in many aspects pertaining to atmospheric chemistry [e.g., *Finlayson-Pitts and Pitts*, 2000; *Jacob*, 1999]. In the troposphere, nitrogen oxides ($NO_x = NO + NO_2$) are involved in the production of ozone and impact on the general oxidizing capacity of the atmosphere, through reactions with carbon monoxide (CO) and organic compounds. Mainly released as NO during combustion (industry, traffic, or biomass burning), lightning, and soil emission and rapidly converted to NO_2, the NO_x are further oxidized in the troposphere to other reactive nitrogen species, including short-lived species (NO_3, HNO_2) and a series of longer-lived species (HNO_3, $CH_3COOONO_2$, HO_2NO_2, N_2O_5). In the stratosphere, NO_x are generated primarily from the dissociation of nitrous oxide (N_2O) and are responsible for the major catalytic odd-oxygen loss processes. In both layers, the principal loss mechanism of NO_x is oxidation to nitric acid (HNO_3) and further deposition in the liquid or the solid phase.

[3] A foremost concern for the chemistry of nitrogen oxides lies in the potential of the longer lived NO_y (NO_y = NO_x + oxidation products) to act as reservoirs for the NO_x in the troposphere, possibly affecting air quality and pollution on regional and global scales through the long-range transport of air pollution [*Kasibhatla et al.*, 1993; *Moxim et al.*, 1996; *Hudman et al.*, 2004]. Ground-based and intensive airborne measurement campaigns have provided strong evidence that peroxyacetyl nitrate ($CH_3COOONO_2$, abbreviated as PAN), with a lifetime of several weeks in the upper troposphere, is a major reservoir of NO_x [*Singh et al.*, 1986; *Moxim et al.*, 1996; *Emmons et al.*, 2000, and references therein; *Zellweger et al.*, 2003; *Parrish et al.*, 2004]. It is present in the outflow of urban or biomass burning plumes, with mixing ratios reaching a few parts per billion by

[1] Spectroscopie de l'Atmosphère, Service de Chimie Quantique et Photophysique, Université Libre de Bruxelles, Brussels, Belgium.
[2] Now at Laboratoire d'Aérologie, UMR 5560 CNRS/Université Paul Sabatier, Observatoire de Midi-Pyrénées, Toulouse, France.
[3] Service d'Aéronomie, Institut Pierre-Simon Laplace, Université Pierre et Marie Curie, Paris, France.
[4] Research Associate with the F.N.R.S., Belgium.

0148-0227/07/2006JD008202

volume near the surface [*Hauglustaine et al.*, 1998; *Emmons et al.*, 2000; *Bey et al.*, 2001; *Staudt et al.*, 2003]. HNO_3 is similarly observed at higher concentrations in the troposphere and is also longer lived (several weeks to a month in the upper troposphere), making it a candidate for the transport of air pollution, possibly regenerating NO_2. [*Chatfield*, 1994; *Lary et al.*, 1997; *Hauglustaine et al.*, 1998]. However, because of its high solubility in water, it is scavenged by rain and its role as an effective reservoir for NO_x remains controversial. Furthermore, chemistry and transport models frequently fail to reproduce the observations [*Hauglustaine et al.*, 1998; *Thakur et al.*, 1999; *Staudt et al.*, 2003]. The scientific community therefore underlines the lack of global observations of HNO_3, required for a detailed partitioning of the NO_y in the troposphere [*Emmons et al.*, 1997; *Emmons et al.*, 2000; *Li et al.*, 2004].

[4] HNO_3 measurements in the troposphere are difficult to perform and relatively sparse. At ground level, the measurements generally rely on gas sampling but the intercomparison between different techniques lead to poor agreement [*Fehsenfeld et al.*, 1998; *Hering et al.*, 1988]. Airborne measurement campaigns have provided the most extensive sets of data, highlighting the vertical distribution of HNO_3 on local and regional scales [*Emmons et al.*, 2000, and references therein; *Miyazaki et al.*, 2003; *Hudman et al.*, 2004]. However, satellite measurements of HNO_3 covering the whole troposphere have not been reported yet. In the stratosphere, HNO_3 vertical distributions can be inferred from the analyses of data collected by limb-sounders, operating either in the infrared [*Irie et al.*, 2006; *Lopez-Puertas et al.*, 2005; *Stiller et al.*, 2005; *Tsidu et al.*, 2005] or microwave [*Santee et al.*, 1999; *Santee et al.*, 2004; *Urban et al.*, 2005] spectral regions. Their analyses have shed light on a series of key processes, particularly in relation to the chemistry in the polar regions [e.g., *Santee et al.*, 2004]. Ground-based Fourier Transform Infrared (FTIR) solar absorption measurements, which sound the entire atmospheric column, enable the retrieval of HNO_3 vertical profiles, but with strong correlations between the troposphere and the stratosphere [e.g., *Vigouroux et al.*, 2007; *Wood et al.*, 2004].

[5] The Michelson Interferometer for Passive Atmospheric Sounding (MIPAS) [*Fischer and Oelhaf*, 1996] and the Atmospheric Chemistry Experiment Fourier Transform Spectrometer (ACE-FTS) [*Bernath et al.*, 2005; *Martin et al.*, 2006] instruments have measured HNO_3 in the upper troposphere and in the stratosphere with a high vertical sensitivity. However, simultaneous measurements of nitric acid global distributions in the whole troposphere and the stratosphere have not been reported.

[6] In this work, we explore for the first time the potential of satellite measurements in the infrared spectral region using a nadir-pointing device for the simultaneous measurement of HNO_3 abundances in the stratosphere and in the entire troposphere. For this purpose, our analysis uses a set of high spectral resolution measurements provided by the Interferometric Monitor of Greenhouse Gases (IMG) instrument, which flew onboard the ADEOS platform. Using 10 successive days of IMG operation in April 1997, we aim, in particular, to derive global tropospheric concentrations with an accuracy allowing the study of regional- and global-scale processes, related, for instance, to the NO_y partitioning during the long-range transport of pollution.

[7] In the next section, the IMG measurements, the retrieval method, and parameters are briefly described. In section 3, the HNO_3 profiles are presented and characterized. The spatial distributions are discussed separately for the stratospheric and tropospheric columns on the global scale. Conclusions and perspective for future applications are drawn in section 4.

2. Measurements and Methods

2.1. Measurements

[8] The Interferometric Monitor for Greenhouse Gases (IMG) mission took place on the ADEOS sun-synchronous, ground track repeat polar-orbiting platform during 10 months between August 1996 and June 1997 [*Kobayashi et al.*, 1999]. The IMG instrument was a high-resolution nadir-viewing Fourier transform spectrometer, with 10-cm optical path difference (OPD). It measured the thermal infrared emission from the Earth atmosphere between 650 and 3000 cm^{-1}, in three separate bands, each corresponding to a 8 × 8-km footprint on the ground. The IMG measurements were taken by a series of six, separated by 86 km each, followed by reference blackbody calibration measurements. The distance between two batches of measurements was 297 km. Routine operations alternated 4 days of measurements with 10 days halt in order to reduce the data flow. The only exception is the period between the 1st and the 10th of April 1997 for which 10 consecutive days of measurements have been made.

[9] In this study, we focus on this time period, described in several other publications [*Clerbaux et al.*, 2001, 2003; *Turquety et al.*, 2002, 2004; *Barret et al.*, 2005]. The analyses are performed on cloud-free scenes, using a filter that relies on the brightness temperature difference between a series of absorption-free channels around 11 and 12 μm. A value of 5 K on the absolute difference of brightness temperatures is taken as the rejection criterion. Noisy spectra were also filtered out with a final filtering based on the root mean square value of the spectral residuals after retrieval.

2.2. Retrieval Method

[10] For the retrievals, we rely on the same method and instrumental parameters as in the study by *Coheur et al.* [2005], which reports on retrievals and validations of ozone vertical profiles at 9.7 μm, also in IMG band 3. The theoretical elements relevant for the present study are briefly recalled hereafter.

[11] We use the "Atmosphit" software (the software is available at http://home.tiscali.be/dhurtma/atmosphit.html), a detailed line-by-line radiative transfer model [e.g., *Barret et al.*, 2005; *Coheur et al.*, 2005], containing ray tracing for various geometries and a retrieval scheme based on the optimal estimation method (OEM) [*Rodgers*, 2000]. According to the latter, an approximation $\hat{x}$ of the true state x (in our case, the HNO_3 vertical profile) can be retrieved from remote-sensing observations using a combination of, on one hand, the measurement vector $\mathbf{y}$ (the IMG radiances) and the measured signal error variance-covariance matrix $\mathbf{S}_\varepsilon$ and, on the other hand, a priori information

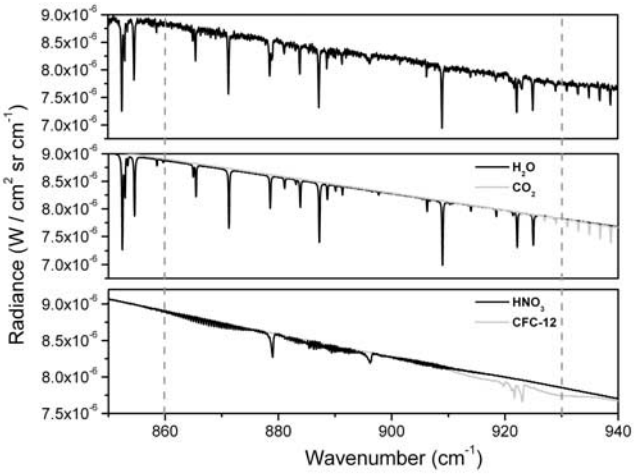

Figure 1. Top: IMG radiance spectrum in the atmospheric window (Pacific Ocean, 4 April 1997). Middle and bottom: Principal contributions from H_2O and CO_2 (middle) and HNO_3 and CFC-12 (bottom) to the observation. The dashed lines indicate the limits of the window selected for the retrievals.

composed of a profile $\boldsymbol{x}_a$ and of its associated variance-covariance matrix $\mathbf{S}_a$.

[12] For a nonlinear problem, the measurement vector can be written as

$$\mathbf{y} = F(\boldsymbol{x}, \boldsymbol{b}) + \varepsilon \tag{1}$$

where F is the forward radiative transfer function, b represents model parameters affecting the measurement, and ε is the measurement noise. The retrieved state $\hat{\boldsymbol{x}}$ is found by iteration as follows:

$$\hat{\boldsymbol{x}}_{i+1} = \boldsymbol{x}_a + (\mathbf{K}_i^T \mathbf{S}_\varepsilon^{-1} \mathbf{K}_i + \mathbf{S}_a^{-1})^{-1} \mathbf{K}_i^T \mathbf{S}_\varepsilon^{-1} \left[\mathbf{y} - F(\hat{\boldsymbol{x}}_i) + \mathbf{K}_i(\hat{\boldsymbol{x}}_i - \boldsymbol{x}_a)\right] \tag{2}$$

with $\mathbf{K}$ being the Jacobian matrix, of elements $\mathbf{K} = \partial\mathbf{y}/\partial\boldsymbol{x}$. As in the work of *Barret et al.* [2005] and *Coheur et al.* [2005], $\mathbf{S}_\varepsilon$ is chosen to be diagonal with identical diagonal elements σ_ε^2 ($\mathbf{S}_\varepsilon = \sigma_\varepsilon^2 I$), where σ_ε is a constraint representing the noise equivalent spectral radiance. The retrieved state is obtained after convergence, when the absolute difference between every element of F modeled at two successive iteration steps, $|F(\hat{\boldsymbol{x}}_{i+1}) - F(\hat{\boldsymbol{x}}_i)|$, is less than a fraction (20%) of σ_ε.

[13] The OEM provides an efficient way for characterizing the retrieved state in terms of vertical sensitivity and error sources. For this purpose, however, the linear approximation needs to be assumed. In this case, the retrieved state is given by [*Rodgers*, 2000]

$$\hat{\boldsymbol{x}} = \boldsymbol{x}_a + \mathbf{A}(\boldsymbol{x} - \boldsymbol{x}_a) + \mathbf{G}(\varepsilon + \mathbf{K}_b(\boldsymbol{b} - \hat{\boldsymbol{b}})) \tag{3}$$

[14] Equation (3) introduces the averaging kernel matrix $\mathbf{A} = \partial\hat{\boldsymbol{x}}/\partial\boldsymbol{x}$ and the gain matrix $\mathbf{G} = \partial\hat{\boldsymbol{x}}/\partial\mathbf{y}$. The rows of $\mathbf{A}$ give the sensitivity of the retrieved profile to the true state. It means that, at a given level, the peak of the function gives the altitude of maximum sensitivity, whereas its full width at half maximum is an estimate of the vertical resolution of the retrieval. The trace of $\mathbf{A}$, known as the degrees of freedom for signal (DOFS), indicates the number of independent values of concentrations that can be retrieved independently on the vertical.

[15] The global error can be computed by considering the difference between the retrieved and the true profiles as follows:

$$\hat{\boldsymbol{x}} - \boldsymbol{x} = (\mathbf{A} - I)(\boldsymbol{x} - \boldsymbol{x}_a) + \mathbf{G}\boldsymbol{e} + \mathbf{G}\mathbf{K}_b(\boldsymbol{b} - \hat{\boldsymbol{b}}) \tag{4}$$

[16] The total error variance-covariance matrix $\mathbf{S}_x$ can then be regarded as the sum of three error terms, related, respectively, to the smoothing of the true profile by the averaging kernel, the measurement noise, and the uncertainties on the model parameters as follows:

$$\mathbf{S}_{\text{total}} = \mathbf{S}_{\text{smoothing}} + \mathbf{S}_{\text{meas}} + \mathbf{S}_{\text{mod.param.}} \tag{5}$$

With

$$\mathbf{S}_{\text{smoothing}} = (\mathbf{A} - I)\mathbf{S}_a(\mathbf{A} - I)^T \tag{6}$$

$$\mathbf{S}_{\text{meas.}} = \mathbf{G}\mathbf{S}_\varepsilon\mathbf{G}^T \tag{7}$$

$$\mathbf{S}_{\text{mod.param.}} = \mathbf{G}\mathbf{K}_b\mathbf{S}_b(\mathbf{G}\mathbf{K}_b)^T \tag{8}$$

In equation (7), $\mathbf{S}_\varepsilon$ is the matrix defined above, which is used as constrain on the measurement, and, in equation (8), $\mathbf{S}_b$ is a matrix accounting for uncertainties on the model parameters (for example, the temperature and the humidity profiles). In our case, both are taken diagonal.

2.3. Data Analysis

[17] For the retrievals, a wide spectral window within IMG band 3 is selected: It extends from 860 to 930 cm^{-1} and encompasses the ν_5 and $2\nu_9$ absorption bands of HNO_3 (Figure 1). Although these bands are not the most intense absorption features of HNO_3 in the thermal infrared, the choice is justified by the absence of strong overlapping absorption features in this spectral region. A priori information ($\boldsymbol{x}_a$ and $\mathbf{S}_a$) was built using a set of monthly (March to June) and latitudinally averaged HNO_3 profiles from the MIPAS instrument (available at http://www.atm.ox.ac.uk/group/mipas/month/) extending from the upper troposphere to 40 km in altitude. The latter were connected to the ground using reference profiles, representative of either remote regions or polluted regions [*Hauglustaine et al.*, 1998]. As shown in Figure 2, the resulting a priori profile is about 1 ppbv near the surface and reaches a maximum of 6.5 ppbv in the stratosphere with, in both altitude regions, significant variability allowed. A value $\sigma_\varepsilon = 4.5 \times 10^{-8}$ W/(cm^2 sr cm^{-1}), close to the expected value of the radiometric noise, is taken as further constrain on the retrievals.

[18] The HNO_3 profiles are retrieved on nine levels, chosen in the middle of layers extending from the ground to 40 km (0–2, 2–5, 5–10, 10–15, 15–20, 20–25, 25–30, 30–35, and 35–40 km). Surface temperature, water

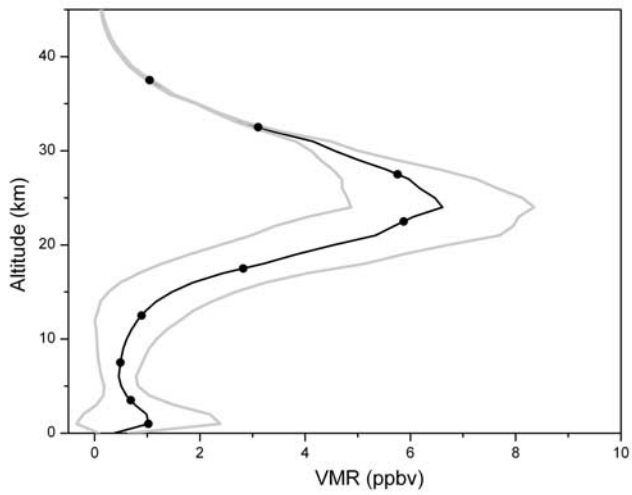

Figure 2. Global HNO_3 a priori profile (black line) and variability (grey lines, square root of the diagonal elements of the variance-covariance matrix) used for the retrievals. The retrieval levels are indicated by black dots.

vapor profile, and CFC-12 total column are adjusted simultaneously.

3. Results and Discussion

3.1. Retrievals and Characterizations

[19] The spectral window chosen for this study lies close to the maximum of the Earth's outgoing radiance, providing measurements with a high signal-to-noise ratio (SNR). An important result which follows is that, despite the weakness of its absorption features, HNO_3 can be successfully retrieved at all latitudes. This is illustrated in Figure 3, which gives the result of the spectral fits at three locations representative of tropical, midlatitude, and polar regions. In the tropics and the midlatitudes, the water vapor lines are strong and interfere with HNO_3 (Figures 3a and 3b), whereas in the cold polar region the amount of water vapor is low and the nitric acid absorption features are easily identified (Figure 3c). In all cases, however, the spectral adjustment is remarkable, with the root mean square (RMS) value of the residual spectra (observed-calculated), being of the same order of magnitude as in the instrument radiometric noise (4.5×10^{-8} W/cm^2 sr cm^{-1}).

[20] For the three examples of Figure 3, we calculate DOFS value ranging from 1.7 (tropical region) to 1.2 (polar

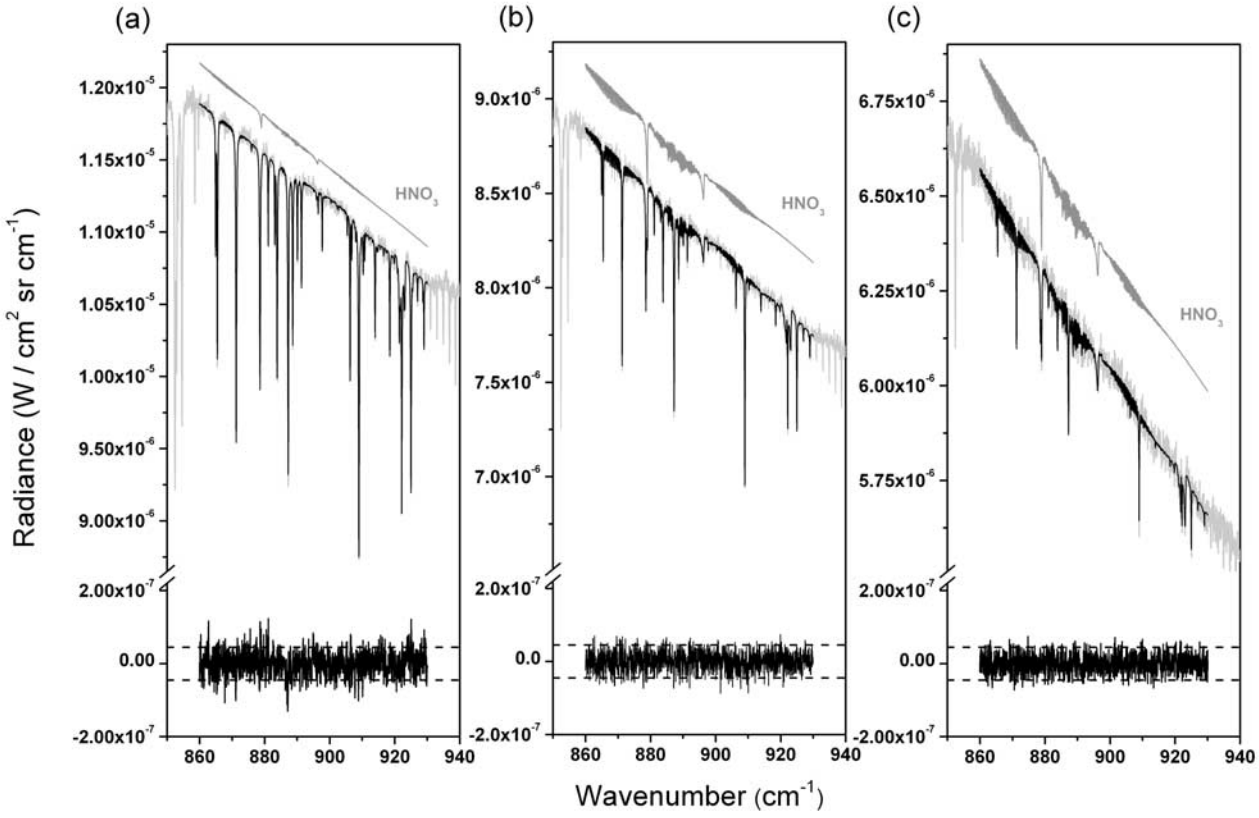

Figure 3. Example of spectral fits for three typical scenes corresponding to (a) tropical, (b) midlatitude, and (c) polar scenes. The light grey and black lines represent the observed and fitted spectra, respectively. The dark grey line is the adjusted HNO_3 contribution and is shifted on the vertical scale for clarification. The residuals (observed-fitted spectra), with associated RMS equal to 3.3×10^{-8}, 2.6×10^{-8}, and 2.5×10^{-8} W/cm^2 sr cm^{-1}, respectively, are also shown and compared to the $\mathbf{S}_\varepsilon$ value selected (4.5×10^{-8} W/(cm^2 sr cm^{-1})) for the retrievals (dashed horizontal lines).

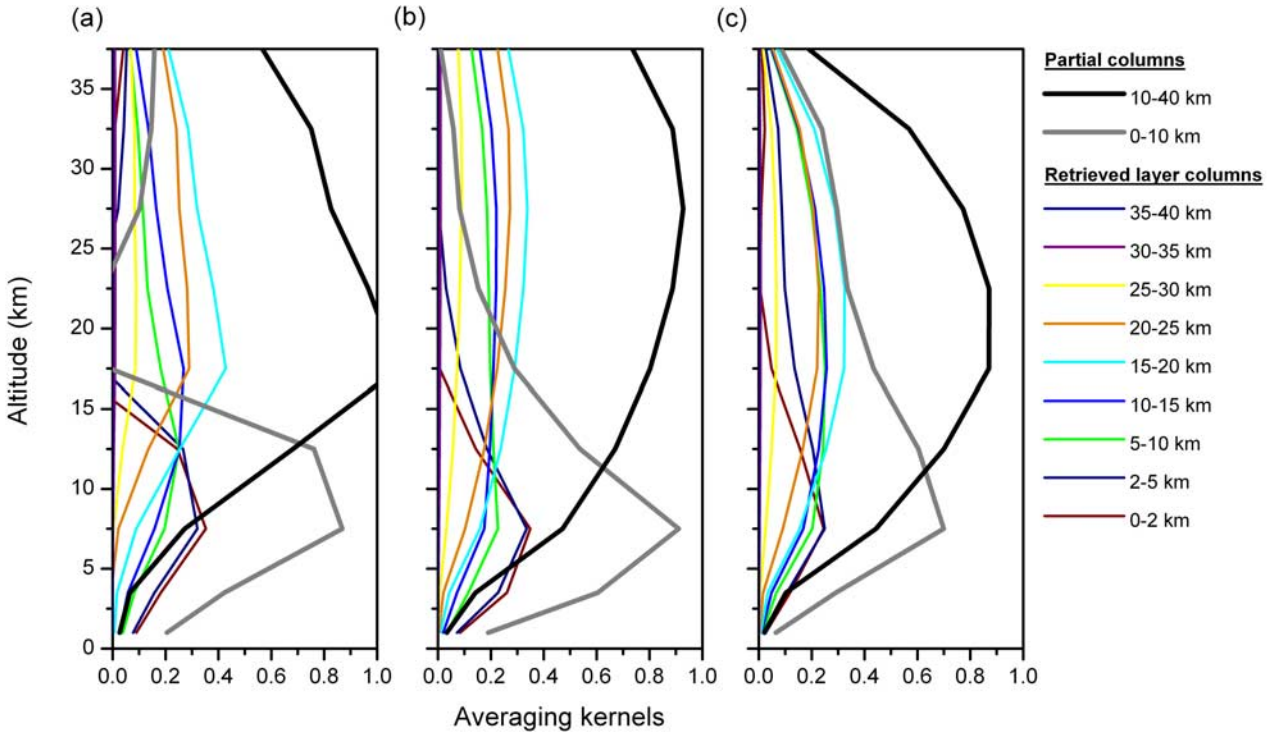

Figure 4. Averaging kernels, in partial column units, for the same three cases as in Figure 3. The averaging kernels for the nine retrieved layers are shown, along those for the 0–10 km (grey) and 10–40 km (black) columns, most representative of the vertical information contained in the measurements.

region). As explained in earlier studies [*Barret et al.*, 2005; *Coheur et al.*, 2005], these differences in the vertical sensitivity are correlated to the surface temperature. The high temperature scenes provide measurements with a higher signal-to-noise ratio, which contain more information on the target species. The averaging kernels corresponding to the three cases, plotted in Figure 4, demonstrate that the measurements provide information on the HNO_3 vertical distribution from the surface up to ~40 km, with a maximum sensitivity in the middle troposphere at about 7 km and in the lower stratosphere between 18 and 30 km. As a result, for the measurements with a DOFS larger than 1, two contributions can partly be separated into a tropospheric (0–10 km) and a stratospheric (10–40 km) column. On the contrary, in the colder polar region where the DOFS is close to one, only the total column is relevant.

[21] A typical error budget is provided in Figure 5. The total error is particularly large near the surface, where it reaches 90% and only provides a modest improvement in comparison with the a priori variability (110% at 1 km). The total error on the profile rapidly drops with altitude to less than 40%. The gain with respect to the prior uncertainty is then remarkable; it is a factor of three in the lower and upper troposphere and even reaches a factor of seven in the middle troposphere and in the lower stratosphere, where the sensitivity is highest. As could be anticipated from the limited vertical sensitivity of the measurements, the calculated total error on the retrieved profile is strongly dominated by the smoothing error which represents the measurement sensitivity to the vertical structure of HNO_3. The other significant contributions to the total error include the measurement error and, to a lesser extent, external errors introduced by uncertainties on the humidity and the temperature profile. The latter never exceed 5%. Other possible sources of errors, such as those caused by uncertainties on the surface parameters (surface temperature and emissivity) and CFC-12 interferences were found to be less than 1%. In terms of columnar amounts, we calculated the total error to be of the order of 25% for the 0 to 40 km column, which is to be compared to an a priori uncertainty of 64%. The error on the 10–40 km column is 10% and improves greatly the prior uncertainty of 65%. Finally, the error on the tropospheric column is about 60%. Despite being relatively large, this value still improves the prior uncertainty (90%) and is also, interestingly, below the accuracy of current atmospheric models [*Hauglustaine et al.*, 1998; *Thakur et al.*, 1999; *Staudt et al.*, 2003]. In spite on the limited accuracy and vertical resolution, the HNO_3 retrievals thus provide significant new information for the improvement of current model simulations.

3.2. Global Distributions

[22] The global distribution of the DOFS for the 10 days of IMG operation analyzed here is shown in Figure 6. Taken globally, the DOFS ranges from 0.7 (cold polar regions) up to 1.8 (hot tropical regions). Within the intertropical belt, a contrast between land and sea surfaces is also observed, with the higher DOFS being measured above the somewhat hotter sea surface. The DOFS is larger than one for most cases. This means that IMG can provide, to some extent, independent tropospheric and stratospheric partial columns

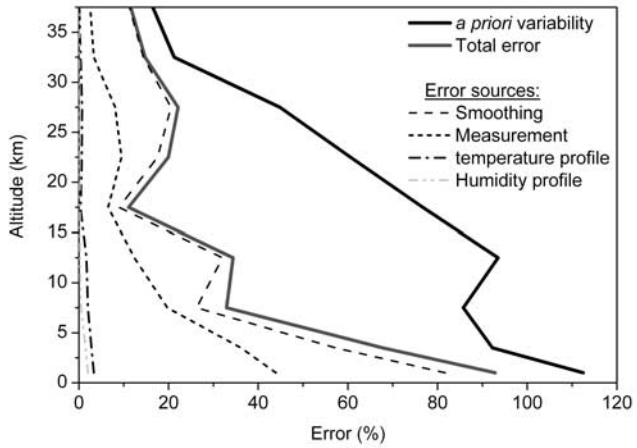

Figure 5. Error profile. The curves are the square root of the diagonal elements of the a priori and posterior error covariance matrices [equations (5) to (8)]. For computing the errors due the temperature and relative humidity profiles, uncertainties of 1 K and 10% were assumed, respectively. The errors due to surface properties (surface temperature and emissivity) and to the uncertainties on the retrieved CFC-12 total columns are negligible and therefore not shown.

of HNO_3. A value of 1.2 for the DOFS is selected as a threshold for this purpose; it is chosen on one hand to exclude the measurements with very strong correlations between the troposphere and the stratosphere while ensuring, on the other hand, that sufficient data are kept for the distribution analyses. The results are presented in Figure 7.

[23] In the stratosphere (Figure 7a), the distribution shows the general patterns expected for the month of April analyzed here. This includes notably enhanced concentrations poleward of 30° in the northern hemisphere and of about 45° in the southern hemisphere, and low abundances within the intertropical belt, where HNO_3 is subject to photolysis due to increased insolation. The measured partial columns range from about 1.2×10^{15} to 3.5×10^{16} molecules cm^{-2} and are in reasonable agreement, considering the different time periods and the likely differences in the reference spectroscopy, with those measured by ground-based FTIR measurements. For instance, *Rinsland et al.* [2003] and *Vigouroux et al.* [2007] reported values between 7×10^{15} and 2.3×10^{16} molecules cm^{-2} in middle and polar latitudes, for a stratospheric and a partial column from 14 to 27 km, respectively. Our results, which show profiles with a stratospheric maximum at 24 km of about 12 ppbv at the South Pole and about 17 ppbv at the North Pole, are also consistent with the range of values (between 10 and 14 ppbv) retrieved from other satellites, at similar time periods [*Santee et al.*, 1998, 1999; *de Zafra and Smyshlyaev*, 2001].

[24] The global distributions of HNO_3 in the troposphere (0–10 km partial column), displayed in Figure 7b, is the most innovative result of this study. Indeed, if one neglects the higher-latitude regions, where the elevated concentrations are likely due to an ineffective separation of tropospheric and stratospheric columns, Figure 7b reveals a series of interesting pattern in terms of NO_x emission and transport. The most remarkable one is the enhanced HNO_3 concentrations measured in the Northern Hemisphere, near the East coast of the United States, central Europe as well as several spots in Asia, which are dominant NO_x source regions [*Richter et al.*, 2006]. Three typical examples of HNO_3 vertical profiles measured in these areas are shown in Figure 8. Compared to the a priori, two are characterized by lower values in the stratosphere and higher values in the troposphere, suggesting that the two partial columns are well decorrelated. Mixing ratios of HNO_3 up to about 2 ppbv are measured in the lower troposphere, in agreement with the results reported by *Hauglustaine et al.* [1998] where the mixing ratios reach 1–4 ppbv. The values for the profile on the east coast of the USA also matches local data, obtained from the ground or airplanes, which give HNO_3 mixing ratio in the range of 1–2 ppbv [*Horowitz et al.*, 1998; *Emmons et al.*, 2000] and even higher [*Neuman et al.*, 2006]. The results for this region support the conclusions of *Horowitz et al.* [1998], who showed that more than half of the NO_x emitted from the north of the USA is exported to the free troposphere as HNO_3. On the contrary, the profile for northern China shows somewhat larger values than those reported by *Bey et al.* [2001] from the analyses

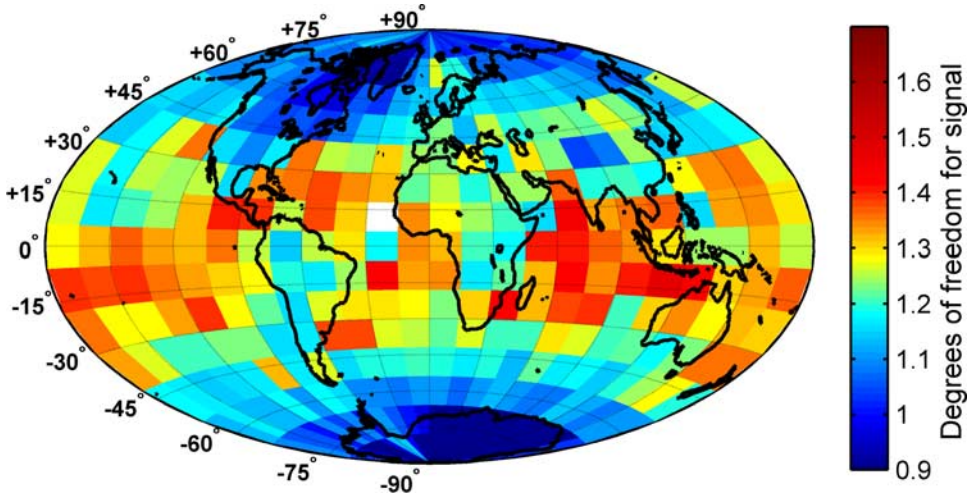

Figure 6. Global distribution of the DOFS. Data are averaged on a 15° × 12° grid.

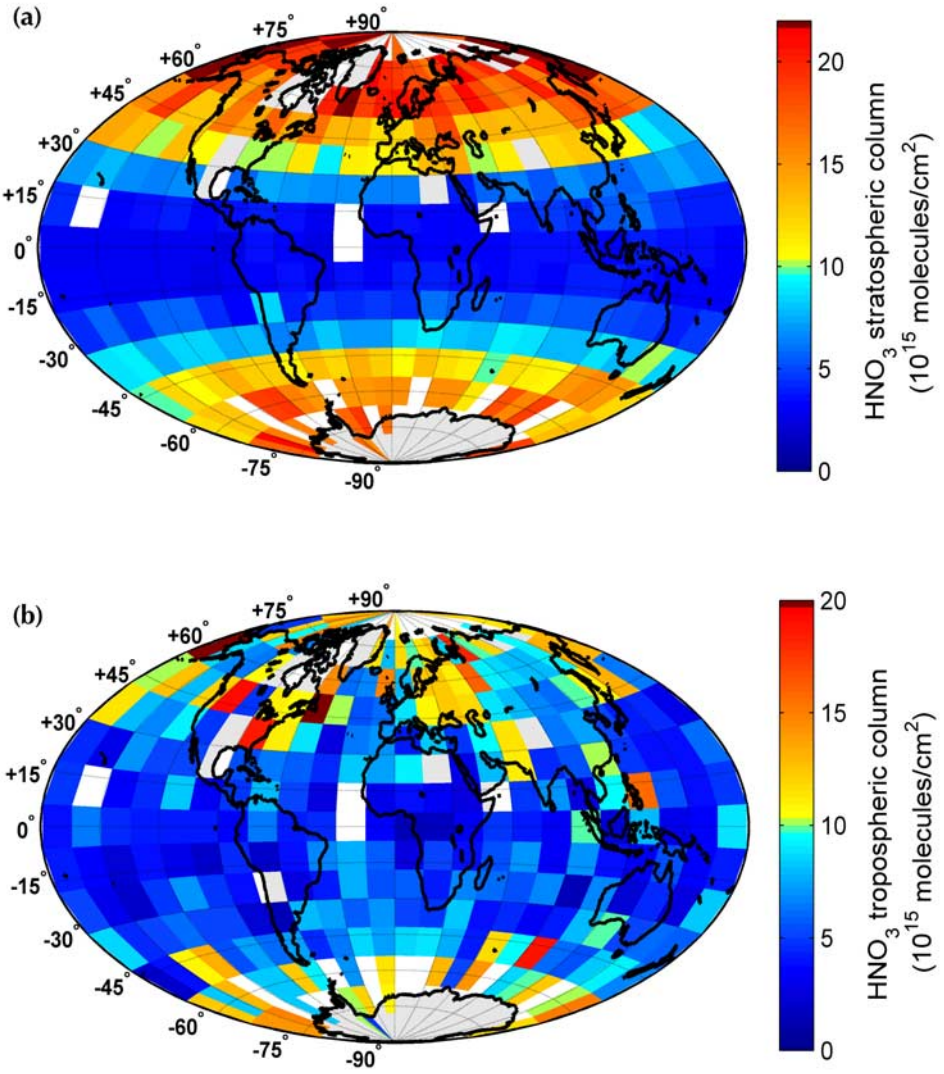

Figure 7. Global distribution of HNO_3 in the stratosphere (10–40 km, top panel) and the troposphere (0–10 km, bottom panel), in 10^{15} molecules cm^{-2}. Only profiles with a DOFS larger than 1.2 are considered. Data are averaged on a 15° × 12° grid.

of the PEM-West B aircraft observations in February–March 1994 (HNO_3 not higher than 500 pptv).

[25] An interesting feature in Figure 7b lies in the observation of elevated HNO_3 columns off the coasts of China, as reported by *Parrish et al.* [2004] and *Hudman et al.* [2004] in their analysis of the transpacific transport of Asian pollution during the PEACE-B and the ITCT 2K2 aircraft campaigns in April–May 2002, as well as above the Atlantic Ocean at northern latitudes. These enhanced HNO_3 abundances in remote areas suggest that the species is transported far from the NO_x source region.

[26] Finally, Figure 7b does not show HNO_3 enhancements within the intertropical belt and especially above the continents (central Africa, southern America, and Asia), although these are regions frequently affected by biomass burning and lightning, both sources of NO_x [*Crutzen and Andreae*, 1990; *Martin et al.*, 2006]. This is likely due to the weak biomass burning activity in April 1997, combined by the fact that HNO_3 can be very effectively removed from the atmosphere because of the steamy conditions in the tropics and the presence of the fire smoke [*Takegawa et al.*, 2003]. The absence of HNO_3 from lightning is probably to be explained by the fact that most of the sources are above 10 km, which is the upper limit considered here for the tropospheric column [*Martin et al.*, 2006].

4. Conclusions and Perspectives

[27] Using the high-spectral resolution infrared measurements of the IMG nadir sounder for 10 successive days in April 1997, we have measured quasi-global distributions of nitric acid in the troposphere and the stratosphere. The results were obtained by retrieving HNO_3 volume mixing ratios on nine levels from the ground up to 40 km in altitude, using a retrieval algorithm that relies on the optimal estimation method. For the retrievals, we have selected a portion of the IMG spectra between 860 and 930 cm^{-1}, which includes the ν_5 and $2\nu_9$ absorption bands of HNO_3.

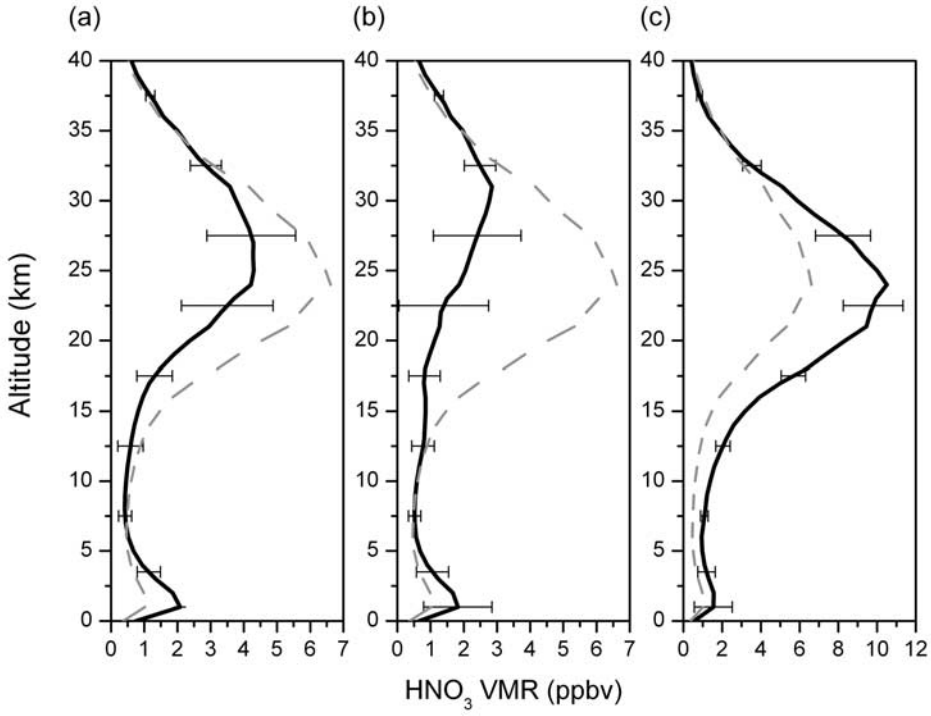

Figure 8. Examples of profiles, with the calculated errors bars, showing high volume mixing ratio of HNO_3 in the troposphere. The panels from left to right correspond, respectively, to measurements (a) in the north Atlantic Ocean off the coast of the USA (36.5° North and 72.5° West), (b) the north-west of India (24.9° North and 70.4° East), and (c) the northeast of China (49.4° North and 133.1° East). The a priori profile is shown in grey dashed line.

A detailed characterization of the retrieved HNO_3 profiles has shown that the measurements contain, except for the coldest regions of the globe, between 1.2 and 1.8 independent pieces of information on the vertical HNO_3 profile, with a sensitivity extending from the ground to about 40 km in altitudes. On the basis of the analysis of the averaging kernels, we have been able to separate two columns, mainly representative of the troposphere (ground–10 km) and the stratosphere (10–40 km). The limited vertical sensitivity of the measurements, especially in the troposphere, causes the total error on the retrieved columns to be dominated by the smoothing error; it ranges from 5% on the 10–40 km to 60% on the ground–10 km but provide, in all cases, improvement with respect to the prior uncertainties. The distribution of HNO_3 in the stratosphere shows the expected general patterns for the month of April, and the measured column values were shown to be in good agreement with ground-based data. The first tropospheric HNO_3 distribution has been presented and discussed. Its analysis reveals regions with enhanced HNO_3 concentrations, up to a few parts per billion by volume in the boundary layer, matching local ground-based or airborne measurements. The regions with elevated HNO_3 in the troposphere have been found in the Northern Hemisphere close to the NO_x source regions and extending toward remote areas. This is consistent with field campaign and model analyses. It suggests that HNO_3 is effectively transported and possibly acts as a reservoir of NO_x. A detailed validation of the data has not been possible due to the lack of correlative observations during the time period considered.

[28] These results open very promising perspectives for the scientific output to be expected from future satellite missions dedicated to the identification and the study of both stratospheric and tropospheric chemical processes. It also adds to the potential of thermal infrared tropospheric sounders to contribute to an in-depth analysis of tropospheric chemistry, air quality, and the transport of air pollution, which was earlier considered to be mainly restricted to the measurements of ozone and carbon monoxide. Among the future instruments that will enable the measurement of global distributions of HNO_3 is the Infrared Atmospheric Sounding Interferometer (IASI), which will be part of the three successive MetOp platforms [*Clerbaux et al.*, 2003; *Turquety et al.*, 2004]. The coarser resolution (0.5 cm^{-1}) of IASI with respect to IMG may, however, not allow the direct retrieval of tropospheric columns. Nevertheless, it is anticipated that the analysis of HNO_3 total columns to be provided by IASI, in conjunction with the NO_2 data products of GOME-2, present onboard the same platform, will improve our understanding of the chemistry and the transport of reactive nitrogen in the troposphere.

[29] **Acknowledgments.** The research was funded by the Fonds National de la Recherche Scientifique (FNRS, Belgium), the Belgian State Federal Office for Scientific, Technical and Cultural Affairs and the European Space Agency (ESA-Prodex arrangement C90-220). Financial support by the "Actions de Recherche Concertées" (Communauté Française de Belgique) is also acknowledged. This work was undertaken in the

framework of the ISSWG (IASI Sounding Science Working Group) activities under the auspices of EUMETSAT (European Organization for the Exploitation of Meteorological Satellites) and CNES (Centre National d'Etudes Spatiales). The authors are grateful to IMGDIS/ERSDAC for providing the IMG level 1 data. Thank also to Tam Hau Nguyen Ba for her contribution to this work.

References

Bernath, P. F., et al. (2005), Atmospheric Chemistry Experiment (ACE): Mission overview, *Geophys. Res. Lett.*, *32*, L15S01, doi:10.1029/2005GL022386.

Barret, B., S. Turquety, D. Hurtmans, C. Clerbaux, J. Hadji-Lazaro, I. Bey, M. Auvray, and P. F. Coheur (2005), Global carbon monoxide vertical distributions from spaceborne high-resolution FTIR nadir measurements, *Atmos. Chem. Phys.*, *5*, 2901–2914.

Bey, I., D. J. Jacob, J. A. Logan, and R. M. Yantosca (2001), Asian chemical outflow to the Pacific in spring: Origins, pathways, and budgets, *J. Geophys. Res.*, *106*, 23,097–23,113.

Chatfield, R. B. (1994), Anomalous HNO_3/NO_x ratio of remote tropospheric air: Conversion of nitric acid to formic acid and NO_x, *Geophys. Res. Lett.*, *21*, 2705–2708.

Clerbaux, C., J. Hadji-Lazaro, D. Hauglustaine, G. Mégie, B. Khattatov, and J. F. Lamarque (2001), Assimilation of carbon monoxide measured from satellite in a three-dimensional chemistry-transport model, *J. Geophys. Res.*, *106*, 15,385–15,394.

Clerbaux, C., J. Hadji-Lazaro, S. Turquety, G. Mégie, and P. F. Coheur (2003), Trace gas measurements from infrared satellite for chemistry and climate applications, *Atmos. Chem. Phys.*, *3*, 1495–1508.

Coheur, P. F., B. Barret, S. Turquety, D. Hurtmans, J. Hadji-Lazaro, and C. Clerbaux (2005), Retrieval and characterization of ozone vertical profiles from a thermal infrared nadir sounder, *J. Geophys. Res.*, *110*, D24303, doi:10.1029/2005JD005845.

Crutzen, P. J., and M. O. Andreae (1990), Biomass burning in the tropics: Impact on atmospheric chemistry and biogeochemical cycles, *Science*, *250*(4988), 1669–1678, doi:101126/science.250.4988.1669.

de Zafra, R., and S. P. Smyshlyaev (2001), On the formation of HNO_3 in the Antarctic mid to upper stratosphere in winter, *J. Geophys. Res.*, *106*, 23,115–23,125.

Emmons, L. K., et al. (1997), Climatologies of NO_x and NO_y: A comparison of data and models, *Atmos. Environ.*, *31*, 1851–1904.

Emmons, L. K., D. A. Hauglustaine, J. F. Müller, M. A. Carroll, G. P. Brasseur, D. Brunner, J. Staehelin, V. Thouret, and A. Marenco (2000), Data composites of airborne observations of tropospheric ozone and its precursors, *J. Geophys. Res.*, *105*, 20,497–20,538.

Fehsenfeld, F. C., L. G. Huey, D. T. Sueper, R. B. Norton, E. J. Williams, F. L. Eisele, R. L. Mauldin, and D. J. Tanner (1998), Ground-based intercomparison of nitric acid measurement techniques, *J. Geophys. Res.*, *103*, 3343–3353.

Finlayson-Pitts, B. J., and J. N. Pitts Jr. (2000), *Chemistry of the upper and lower atmosphere: theory, experiments and applications*, Elsevier, New York.

Fischer, H., and H. Oelhaf (1996), Remote sensing of vertical profiles of atmospheric trace constituents with MIPAS limb-emission spectrometers, *Appl. Opt.*, *35*, 2787–2796.

Hauglustaine, D. A., G. P. Brasseur, S. Walters, P. J. Rasch, J.-F. Müller, L. K. Emmons, and M. A. Carroll (1998), MOZART, a global chemical transport model for ozone and related chemical tracers, *J. Geophys. Res.*, *103*, 28,291–28,335.

Hering, S. V., et al. (1988), The nitric acid shootout: Field comparison of measurement methods, *Atmos. Environ.*, *22*, 1519–1539.

Horowitz, L. W., J. Liang, G. M. Gardner, and D. J. Jacob (1998), Export of reactive nitrogen from North America during summertime: Sensitivity to hydrocarbon chemistry, *J. Geophys. Res.*, *103*, 13,451–13,476.

Hudman, R. C., et al. (2004), Ozone production in transpacific Asian pollution plumes and implications for ozone air quality in California, *J. Geophys. Res.*, *109*, D23S10, doi:10.1029/2004JD004974.

Irie, H., et al. (2006), Validation of stratospheric nitric acid profiles observed by Improved Limb Atmospheric Spectrometer (ILAS)-II, *J. Geophys. Res.*, *111*, D11S03, doi:10.1029/2005JD006115.

Jacob, D. J. (1999), *Introduction to atmospheric chemistry*, Princeton Univ. Press, Princeton, N. J.

Kasibhatla, P. S., H. Levy, and W. J. Moxim (1993), Global NO_x, HNO_3, PAN, and NO_y distributions from fossil-fuel combustion emissions: A model study, *J. Geophys. Res.*, *98*, 7165–7180.

Kobayashi, H., A. Shimota, K. Kondo, E. Okumura, Y. Kameda, H. Shimoda, and T. Ogawa (1999), Development and evaluation of the interferometric monitor for greenhouse gases: A high-throughput Fourier-transform infrared radiometer for nadir Earth observation, *Appl. Opt.*, *38*, 6801–6807.

Lary, D. J., A. M. Lee, R. Toumi, M. J. Newchurch, M. Pirre, and J. B. Renard (1997), Carbon aerosols and atmospheric photochemistry, *J. Geophys. Res.*, *102*, 3671–3682.

Li, Q., D. J. Jacob, J. W. Munger, and R. M. Yantosca (2004), Export of NO_y from the North American boundary layer: Reconciling aircraft observations and global model budgets, *J. Geophys. Res.*, *109*, D02313, doi:10.1029/2003JD004086.

Lopez-Puertas, M., B. Funke, S. Gil-Lopez, T. von Clarmann, G. P. Stiller, M. Hopfner, S. Kellmann, G. M. Tsidu, H. Fischer, and C. H. Jackman (2005), HNO_3, N_2O_5, and $ClONO_2$ enhancements after the October–November 2003 solar proton events, *J. Geophys. Res.*, *110*, A09S44, doi:10.1029/2005JA011051.

Martin, R. V., B. Sauvage, I. Folkins, C. E. Sioris, C. Boone, P. Bernath, and J. Ziemke (2006), Space-based constraints on the production of nitric oxide by lightning, *J. Geophys. Res.*, *112*, D09309, doi:10.1029/2006JD007831.

Miyazaki, Y., et al. (2003), Synoptic-scale transport of reactive nitrogen over the western Pacific in spring, *J. Geophys. Res.*, *108*(D20), 8788, doi:10.1029/2002JD003248.

Moxim, W. J., H. Levy, and P. S. Kasibhatla (1996), Simulated global tropospheric PAN: Its transport and impact on NO_x, *J. Geophys. Res.*, *101*, 12,621–12,638.

Neuman, J. A., et al. (2006), Reactive nitrogen transport and photochemistry in urban plumes over the North Atlantic Ocean, *J. Geophys. Res.*, *111*, D23S54, doi:10.1029/2005JD007010.

Parrish, D. D., Y. Kondo, O. R. Cooper, C. A. Brock, D. A. Jaffe, M. Trainer, T. Ogawa, G. Hübler, and F. C. Fehsenfeld (2004), Intercontinental Transport and Chemical Transformation 2002 (ITCT 2k2) and Pacific Exploration of Asian Continental Emission (PEACE) experiments: An overview of the 2002 winter and spring intensives, *J. Geophys. Res.*, *109*, D23S01, doi:10.1029/2004JD004980.

Richter, A., J. P. Burrows, H. Nüb, C. Granier, and U. Niemeier (2006), Increase in tropospheric nitrogen dioxide over China observed from space, *Nature*, *437*, 129–132.

Rinsland, C. P., D. K. Weisenstein, M. K. W. Ko, C. J. Scott, L. S. Chiou, E. Mahieu, R. Zander, and P. Demoulin (2003), Post-Mount Pinatubo eruption ground-based infrared stratospheric column measurements of HNO_3, NO, and NO_2 and their comparison with model calculations, *J. Geophys. Res.*, *108*(D15), 4437, doi:10.1029/2002JD002965.

Rodgers, C. D. (2000), *Inverse Methods for Atmospheric Sounding: Theory and Practice*, World Sci., Hackensack, N. J.

Santee, M. L., A. Tabazadeh, G. L. Manney, R. J. Salawitch, L. Froidevaux, W. G. Read, and J. W. Waters (1998), UARS Microwave Limb Sounder HNO_3 observations: Implications for Antarctic polar stratospheric clouds, *J. Geophys. Res.*, *103*, 13,285–13,313.

Santee, M. L., G. L. Manney, L. Froidevaux, W. G. Read, and J. W. Waters (1999), Six years of UARS Microwave Limb Sounder HNO_3 observations: Seasonal, interhemispheric, and interannual variations in the lower stratosphere, *J. Geophys. Res.*, *104*, 8225–8246.

Santee, M. L., G. L. Manney, N. J. Livesey, and W. G. Read (2004), Three-dimensional structure and evolution of stratospheric HNO_3 based on UARS Microwave Limb Sounder measurements, *J. Geophys. Res.*, *109*, D15306, doi:10.1029/2004JD004578.

Singh, H. B., L. J. Salas, and W. Viezee (1986), Global distribution of peroxyacetyl nitrate, *Nature*, *321*, 588–591.

Staudt, A. C., D. J. Jacob, F. Ravetta, J. A. Logan, D. Bachiochi, T. N. Krishnamurti, S. Sandholm, B. Ridley, H. B. Singh, and B. Talbot (2003), Sources and chemistry of nitrogen oxides over the tropical Pacific, *J. Geophys. Res.*, *108*(D2), 8239, doi:10.1029/2002JD002139.

Stiller, G. P., et al. (2005), An enhanced HNO_3 second maximum in the Antarctic midwinter upper stratosphere 2003, *J. Geophys. Res.*, *110*, D20303, doi:10.1029/2005JD006011.

Takegawa, N., et al. (2003), Removal of NO_x and NO_y in biomass burning plumes in the boundary layer over northern Australia, *J. Geophys. Res.*, *108*(D10), 4308, doi:10.1029/2002JD002505.

Thakur, A. N., H. B. Singh, P. Mariani, Y. Chen, Y. Wang, D. J. Jacob, G. Brasseur, J.-F. Müller, and M. Lawrence (1999), Distribution of reactive nitrogen species in the remote free troposphere: Data and model comparisons, *Atmos. Environ.*, *33*, 1403–1422.

Tsidu, G. M., et al. (2005), NO_y from Michelson Interferometer for Passive Atmospheric Sounding on Environmental Satellite during the Southern Hemisphere polar vortex split in September/October 2002, *J. Geophys. Res.*, *110*, D11301, doi:10.1029/2004JD005322.

Turquety, S., J. Hadji-Lazaro, and C. Clerbaux (2002), First satellite ozone distributions retrieved from nadir high-resolution infrared spectra, *Geophys. Res. Lett.*, *29*(24), 2198, doi:10.1029/2002GL016431.

Turquety, S., J. Hadji-Lazaro, C. Clerbaux, D. A. Hauglustaine, S. A. Clough, V. Casse, P. Schlussel, and G. Mégie (2004), Operational trace gas retrieval algorithm for the Infrared Atmospheric Sounding Interferometer, *J. Geophys. Res.*, *109*, D21301, doi:10.1029/2004JD004821.

Urban, J., et al. (2005), Odin/SMR limb observations of stratospheric trace gases: Level 2 processing of ClO, N_2O, HNO_3, and O_3, *J. Geophys. Res.*, *110*, D14307, doi:10.1029/2004JD005741.

Vigouroux, C., et al. (2007), Comparisons between ground-based FTIR and MIPAS N_2O and HNO_3 profiles before and after assimilation in BASCOE, *Atmos. Chem. Phys.*, *7*, 377–396.

Wood, S. W., R. L. Batchelor, A. Goldman, C. P. Rinsland, B. J. Connor, F. J. Murcray, T. M. Stephen, and D. N. Heuff (2004), Ground-based nitric acid measurements at Arrival Heights, Antarctica, using solar and lunar Fourier transform infrared observations, *J. Geophys. Res.*, *109*, D18307, doi:10.1029/2004JD004665.

Zellweger, C., J. Forrer, P. Hofer, S. Nyeki, B. Schwarzenbach, E. Weingartner, M. Ammann, and U. Baltensperger (2003), Partitioning of reactive nitrogen (NO_y) and dependence on meteorological conditions in the lower free troposphere, *Atmos. Chem. Phys.*, *3*, 779–796.

B. Barret, C. Clerbaux, P.-F. Coheur, H. Herbin, D. Hurtmans, and C. Wespes, Spectroscopie de l'Atmosphère, Service de Chimie Quantique et Photophysique, Université Libre de Bruxelles, Brussels, Belgium. (pfcoheur@ulb.ac.be)

J. Hadji-Lazaro and S. Turquety, Service d'Aéronomie, Institut Pierre-Simon Laplace, Université Pierre et Marie Curie, Paris, France.